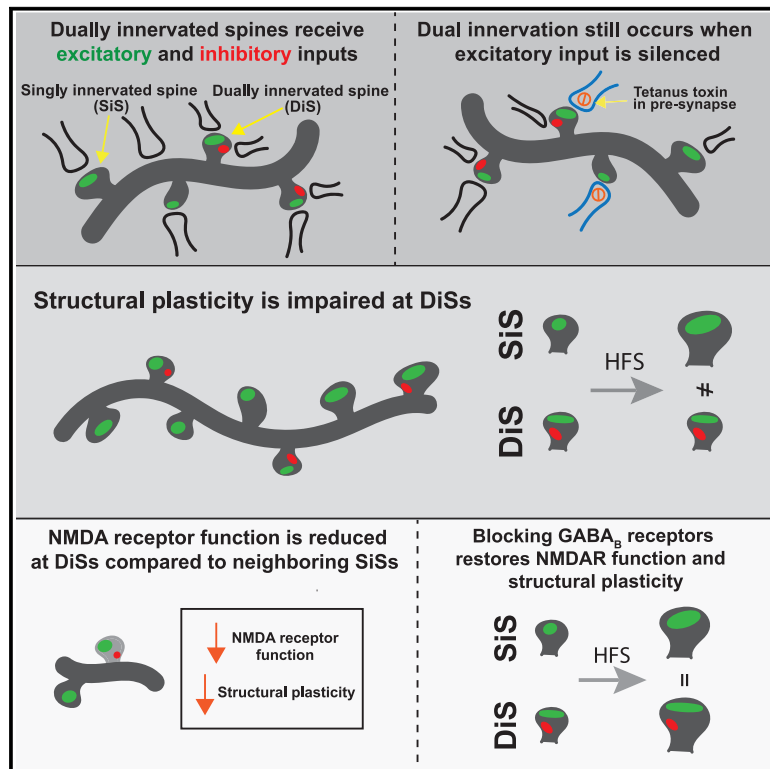


Neuron

Dually innervated dendritic spines develop in the absence of excitatory activity and resist plasticity through tonic inhibitory crosstalk

Graphical abstract



Authors

Mason S. Kleinjan, William C. Buchta, Roberto Ogelman, ..., Kristen M. Harris, Won Chan Oh, Matthew J. Kennedy

Correspondence

wonchan.oh@cuanschutz.edu (W.C.O.), matthew.kennedy@cuanschutz.edu (M.J.K.)

In brief

Kleinjan et al. demonstrate that formation of hippocampal dually innervated spines (DiSs) occurs early in development and does not require excitatory input. NMDA receptor function and structural plasticity are impaired at DiSs. These effects are mediated through tonic GABA_B receptor signaling and may contribute to long-term DiS stability.

Highlights

- DiSs develop early in spinogenesis, independent of excitatory input
- DiSs have reduced structural plasticity compared to SiSs
- Reduced DiS plasticity is mediated through GABA_BR/NMDAR crosstalk
- Reduced plasticity may contribute to long term stability of DiSs

Report

Dually innervated dendritic spines develop in the absence of excitatory activity and resist plasticity through tonic inhibitory crosstalk

Mason S. Kleinjan,¹ William C. Buchta,¹ Roberto Ogelman,¹ In-Wook Hwang,¹ Masaaki Kuwajima,³ Dusten D. Hubbard,³ Dean J. Kareemo,¹ Olga Prikhodko,¹ Samantha L. Olah,¹ Luis E. Gomez Wulschner,¹ Wickliffe C. Abraham,⁴ Santos J. Franco,² Kristen M. Harris,³ Won Chan Oh,^{1,*} and Matthew J. Kennedy^{1,5,*}

¹Department of Pharmacology, University of Colorado School of Medicine, Aurora, CO 80045, USA

²Department of Pediatrics, University of Colorado School of Medicine, Aurora, CO 80045, USA

³Department of Neuroscience, University of Texas at Austin, Austin, TX 78712, USA

⁴Department of Psychology, Brain Health Research Centre, University of Otago, Dunedin, New Zealand

⁵Lead contact

*Correspondence: wonchan.oh@cuanschutz.edu (W.C.O.), matthew.kennedy@cuanschutz.edu (M.J.K.)

<https://doi.org/10.1016/j.neuron.2022.11.002>

SUMMARY

Dendritic spines can be directly connected to both inhibitory and excitatory presynaptic terminals, resulting in nanometer-scale proximity of opposing synaptic functions. While dually innervated spines (DiSs) are observed throughout the central nervous system, their developmental timeline and functional properties remain uncharacterized. Here we used a combination of serial section electron microscopy, live imaging, and local synapse activity manipulations to investigate DiS development and function in rodent hippocampus. Dual innervation occurred early in development, even on spines where the excitatory input was locally silenced. Synaptic NMDA receptor currents were selectively reduced at DiSs through tonic GABA_B receptor signaling. Accordingly, spine enlargement normally associated with long-term potentiation on singly innervated spines (SiSs) was blocked at DiSs. Silencing somatostatin interneurons or pharmacologically blocking GABA_BRs restored NMDA receptor function and structural plasticity to levels comparable to neighboring SiSs. Thus, hippocampal DiSs are stable structures where function and plasticity are potentially regulated by nanometer-scale GABAergic signaling.

INTRODUCTION

A subset of dendritic spines, the primary sites of excitatory synaptic connectivity in the central nervous system, are contacted by both an excitatory and an inhibitory presynaptic terminal.^{1,2} Dually innervated spines (DiSs) have been observed on principal neurons throughout the neocortex, where they represent up to 25%–30% of spine synapses and account for approximately one-third of total dendritic inhibitory inputs.^{1,3–6} While DiSs are widely observed, whether they are functionally distinct from neighboring, singly innervated spines (SiSs) is unclear. DiSs contain inhibitory and excitatory postsynaptic specializations responsible for anchoring GABA and glutamate receptors in closely spaced, but discrete, spine subdomains. Longitudinal *in vivo* imaging revealed that DiSs on cortical pyramidal neurons are larger and more stable than neighboring SiSs.^{7,8} A different study demonstrated that the number of DiSs in the somatosensory cortex increases following whisker stimulation.⁹ Together, these observations suggest that DiSs may develop from SiSs

following activity-dependent forms of plasticity such as long-term potentiation (LTP), hallmarks of which are spine growth and stabilization.^{10,11} However, it is unclear whether synaptic activity and/or plasticity are required for DiS development or maintenance.

Once formed, DiSs are particularly well suited for synaptic crosstalk signaling between excitatory and inhibitory synapses. For example, GABA_A receptors (GABA_ARs) and GABA_B receptors (GABA_BRs) can potentially modulate excitatory function through signaling pathways regulating N-methyl-D-aspartic acid receptor (NMDAR) function.^{12–14} While this type of synaptic crosstalk is likely to be amplified within the femtoliter confines of a dendritic spine, how spine function and plasticity are influenced by an adjoining inhibitory input remains unclear. Here we use a combination of three-dimensional reconstruction through serial section electron microscopy (3DEM), live imaging, single synapse silencing techniques, and neurotransmitter uncaging to characterize the development, function, and plasticity of DiSs.

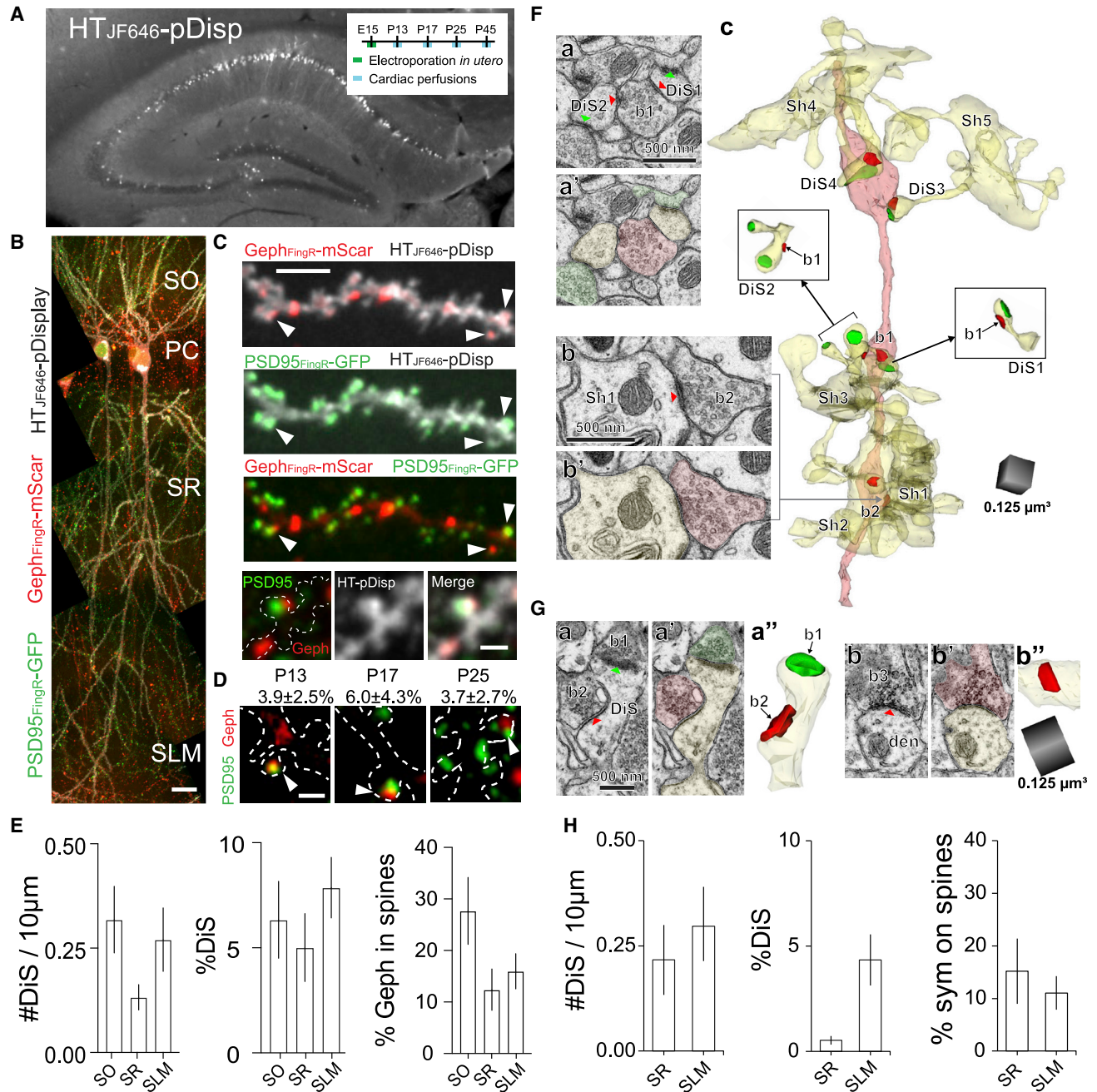


Figure 1. DiSs are present in all layers of hippocampus

(A) Shown is a coronal hippocampal brain section from a P45 mouse that was embryonically electroporated with HT-pDisp, Geph_{FingR}-mScar, and PSD95_{FingR}-GFP (only HT-pDisp channel is shown).

(B) Image of hippocampal CA1 pyramidal cells expressing postsynaptic reporters Geph_{FingR}-mScar (red) and PSD95_{FingR}-GFP (green) and morphology reporter HT_{JF646}-pDisp (gray). Stratum pyramidale, SP; stratum oriens, SO; stratum radiatum, SR; stratum lacunosum moleculare, SLM. Scale bar represents 20 µm.

(C) Zoomed images from (B) showing a dendritic branch with spines positive for both Geph_{FingR}-mScar (red) and PSD95_{FingR}-GFP (green) (arrowheads). A magnified image of a DiS from a different dendrite is shown (bottom row). Scale bars represent 5 µm, 1 µm.

(D) Example images of DiSs at different developmental timepoints. Percentages of total spines that are dually innervated are noted above. N = 40–45 neurons from 10 slices from 6 mice. Scale bar represents 1 µm.

(E) Quantification (mean ± SEM) of DiSs/10 µm of dendrite (left); percent of total spines with both PSD95 and Geph signal (middle); and the fraction of total Geph puncta in spines (right) are plotted for each layer. Data are taken from P45 mice. N = 35–40 neurons from 5 slices from 2 mice.

(F) (a and a') Electron microscopy (EM) image from SR showing two DiSs (DiS1 and DiS2 in a; yellow highlighting in a') making symmetric synapses (red arrowheads in a) with a presynaptic bouton containing pleomorphic vesicles (b1 in a; red in a'). Each DiS makes an asymmetric synapse (green arrowheads in a) with

(legend continued on next page)

RESULTS

DiSs form in hippocampus early during spinogenesis *in vivo* and *in vitro*

We characterized the development and activity dependence of DiS formation, focusing on CA1 pyramidal neurons of the hippocampus, with their well-defined synaptic connectivity and plasticity mechanisms. DiSs were visualized by electroporating embryonic mice (age embryonic day [E]15.5) with intrabody probes (FingRs) that label endogenous gephyrin (fused to mScarlet; Geph_{FingR}-mScar) and PSD95 (fused to green fluorescent protein [GFP]; PSD95_{FingR}-GFP).¹⁵ The plasma membrane marker pDisplay fused to Halotag (HT-pDisp) was used to visualize morphology with JF646 dye.¹⁶ Electroporated hippocampal CA1 pyramidal neurons were imaged by confocal microscopy in perfusion-fixed sections prepared at different ages (postnatal day [P]13, 17, 25, and 45) (Figures 1A–1D). At P45, spines harboring both Geph_{FingR}-mScar and PSD95_{FingR}-GFP signal were observed in stratum oriens (SO; 4%–7% of all spines), stratum radiatum (SR; 3%–6% of all spines), and stratum lacunosum moleculare (SLM; 6%–9% of all spines) (Figures 1B–1D). DiSs accounted for a significant proportion of total dendritic gephyrin puncta (SO, 21%–34%; SR, 9%–16%; SLM, 13%–19%) (Figure 1E). Surprisingly, a similar fraction of DiSs were observed at P13, when dendritic spines are just beginning to form (Figure 1D).

Because fluorescence imaging only reports postsynaptic specializations, DiSs were also characterized through 3DEM using datasets from adult rat hippocampal area CA1. Symmetric synapses (presumably inhibitory) were defined as having thin pre- and postsynaptic thickenings and pleomorphic presynaptic vesicles. Asymmetric synapses (presumably excitatory) had a thick postsynaptic density (PSD) and round presynaptic vesicles. DiSs had both symmetric and asymmetric synapses (Figures 1Fa–a' and 1Ga–a'), although most symmetric synapses were located on dendritic shafts (Figures 1Fb–b' and 1Gb–b'). DiSs accounted for $0.53\% \pm 0.20\%$ of all spines along dendrites in SR and $4.35\% \pm 1.22\%$ in SLM (Figure 1H). The high total spine density in SR of adult rat CA1 accounts for the small fraction of DiSs observed in this layer compared to the confocal imaging, where total spines are likely undercounted. Nevertheless, the density of DiSs in SLM and the overall fraction of symmetric synapses on spines in both SR and SLM are remarkably similar to the confocal imaging data (Figure 1E). In SR and SLM, asymmetric synapse size did not differ significantly between SiSs and DiSs, nor did the size of symmetric synapses located on spines or shafts (Figures S1A and S1B).

We also investigated whether DiSs form in *ex vivo* preparations, which allow for more controlled experimental manipulations. Indeed, we observed Geph/PSD95-positive spines in organotypic hippocampal slices and dissociated cultures. Geph/PSD95-positive spines were associated with presynaptic vesicular GABA transporter (vGAT), contained functional GABA_A receptors, and developed over a similar time course as *in vivo*. (Figures S1C–S1H).

DiS formation in hippocampus does not require excitatory synaptic activity

In cortex, DiSs are dynamically regulated by experience,^{8,9} but it remains unknown if excitatory input is required for DiS formation and/or maintenance. We generated an adeno-associated virus (AAV) encoding the catalytic light chain of tetanus neurotoxin (TeNT_{LC}) to constitutively block presynaptic neurotransmitter release, along with synaptophysin-halotag (Sph-HT) to identify TeNT_{LC}-expressing terminals. This general approach has been shown previously to disrupt presynaptic glutamate release but does not prevent postsynaptic spine development.^{17–22} The efficacy of our Sph-HT-T2A-TeNT_{LC} AAV was confirmed in rat organotypic slices and primary cultured neurons by VAMP2 staining, Fei-Mao (FM) dye loading, and whole-cell recordings (Figures S2A–S2D).

A subset of CA3 principal neurons in rat organotypic hippocampal slices was infected with Sph-HT-T2A-TeNT_{LC} AAV immediately following dissection at P4–5 (Figure 2A). At equivalent postnatal day (EP; postnatal day of slice preparation + days *in vitro*) 13–14, slices were biolistically transfected with Geph_{FingR}-GFP along with tdTomato (tdTom). CA1 pyramidal neurons expressing Geph_{FingR}-GFP/tdTom (the recipients of excitatory inputs from CA3) were imaged 1–2 days later (Figure 2A). The low viral titer achieved sparse (<10%) infection of CA3 neurons such that spines with inactive or unperturbed terminals could be compared on the same cell (Figure 2B). The number of DiSs was not significantly different in slices infected with Sph-HT-T2A-TeNT_{LC} AAV vs. uninfected controls (Figure 2Bi). Surprisingly, silenced terminals appeared directly associated with DiSs. The fraction of DiSs associated with a silenced presynaptic terminal was not significantly different from the fraction of total spines contacted by a silenced input (Figure 2Bii). Likewise, spine Geph_{FingR} signal was not significantly different at DiSs associated with an active or inactive terminal (Figure 2Biii).

To confirm inactivated terminals were directly connected to visualized postsynaptic spines, we used a modified “enhanced GFP reconstitution across synaptic partners” (eGRASP) approach²³ (Figure 2C). An AAV was generated that expresses

a bouton (green highlighting in a') containing round vesicles. (b and b') EM image showing a symmetric synapse (red arrowhead in b) on shaft of another dendrite (yellow in b') with the same presynaptic axon as in a and a' (b2 in b; red in b'). (c) 3D reconstruction of an axon (light red) forming symmetric synapses (red) with five different dendrites (Sh1–5; light yellow). Insets show 3D reconstructions of DiS1 and DiS2 seen in a and a'. DiS2 is a dually innervated branch of a branched spine (excitatory PSDs are rendered in green). The shaft (Sh1) symmetric synapse shown in b and b' is indicated by the gray arrow (b2).

(G) (a and a') EM image from SLM showing a DiS (a; yellow in a') forming a symmetric synapse (red arrowhead in a) with a presynaptic bouton containing pleomorphic vesicles (b2 in a; red in a') and an asymmetric synapse (green arrowheads in a) with a bouton containing round vesicles (b1 in a; green in a'). (a') 3D reconstruction of the DiS shown in a and a'. (b and b') EM image showing a symmetric synapse (red arrowhead in b) on dendritic shaft (yellow in b') with a presynaptic bouton (b3 in b; red in b'). Scale bar in a applies to a', b, and b'. Scale cube in b' also applies to a'.

(H) Quantification (mean \pm SEM) of DiSs in 3D EM reconstructions plotted as the number of DiSs/10 μ m of dendrite length (left), DiSs as a fraction of all spines in SR ($0.53\% \pm 0.20\%$) and SLM ($4.35\% \pm 1.22\%$) (middle), and the fraction of all symmetric synapses located on spines (right). N = 31 (SR) or 36 (SLM) dendrites from three rats for SR and two for SLM.

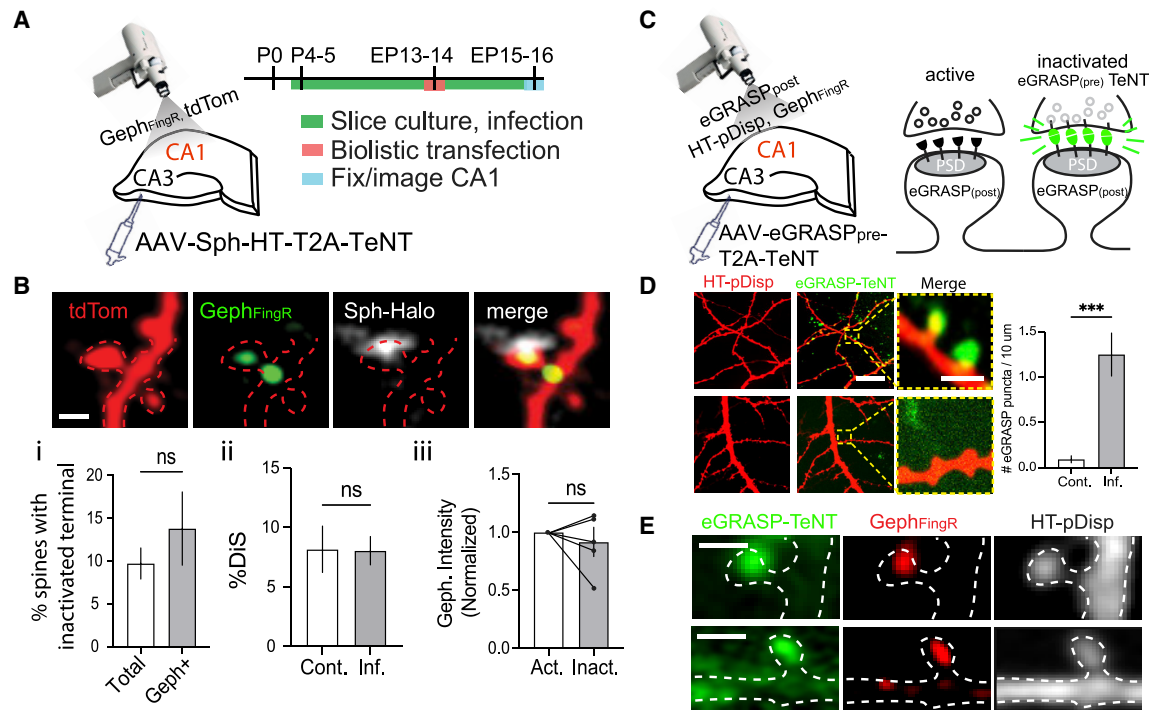


Figure 2. DiS formation does not require excitatory input

(A) Experimental strategy for inactivation of CA3 inputs to CA1. Organotypic hippocampal slices were infected in CA3 with low titer AAV Sph-HT-T2A-TeNT_{LC} immediately following preparation on P5. The slices were biolistically transfected on EP13-15 with tdTom and Geph_{FingR}-GFP. Transfected CA1 pyramidal neurons were imaged to identify DiSs and inactivated terminals.

(B) Representative example of a spine (red) with Geph signal (green) associated with a TeNT-expressing presynaptic terminal (Sph-HT, gray). Graphs (bottom row) plot (i) the fraction of total or gephyrin-positive spines with an inactivated presynaptic terminal (n.s., not significant, Student's t test), (ii) the percentage of total spines that were dually innervated in infected and non-infected slices (n.s., not significant, Student's t test), (iii) the Geph_{FingR}-GFP intensity at TeNT-inactivated DiSs normalized to active DiSs from the same neuron (n.s., not significant, paired Student's t test). n = 5 slices from 2 different animals (Cont.); n = 11 slices from 4 different animals (Inf.). Scale bar represents 1 μm.

(C) Strategy for TeNT-modified eGRASP. Organotypic hippocampal slices were infected in CA3 with eGRASP_{pre}-T2A-TeNT_{LC} AAV immediately following preparation. Slices were then biolistically transfected on EP13-15 with eGRASP_{post}, Geph_{FingR}-mScar, and HT-pDisp to visualize DiSs in CA1 neurons. GFP signal appears at contacts made between transfected postsynaptic cells and inactivated terminals from infected presynaptic cells.

(D) GFP signal is observed in slices infected with eGRASP_{pre}-T2A-TeNT_{LC} and transfected with eGRASP_{post} (top row). No signal was detected in slices not infected with eGRASP_{pre}-T2A-TeNT_{LC} (bottom row, display was increased to highlight lack of eGRASP signal), ***p < 0.001, Student's t test. n = 6 neurons from 6 slices from at least 2 different animals. Scale bars represent 20 μm, 1 μm magnified images.

(E) Examples of eGRASP-labeled and Geph_{FingR}-positive spines. Scale bar represents 1 μm.

presynaptic eGRASP (eGRASP_{pre}) along with TeNT_{LC} (eGRASP_{pre}-T2A-TeNT_{LC}). CA3 pyramidal neurons were sparsely infected with eGRASP_{pre}-T2A-TeNT_{LC} at P5. At EP13-14, slices were transfected with Geph_{FingR}-mScar, HT-pDisp, Cre, and postsynaptic eGRASP (eGRASP_{post}) and imaged 12-24 h later. Reconstituted GFP signal only appears between silenced terminals and spines from cells expressing Geph_{FingR}-mScar/HT-pDisp/Cre/eGRASP_{post} (Figure 2C). In slices expressing both pre- and postsynaptic eGRASP, but not controls, reconstituted GFP signal was observed at gephyrin-containing spines (Figures 2D and 2E). Together, these results indicate that the formation and maintenance of DiSs does not require ongoing activity of the associated excitatory terminal.

Structural plasticity is impaired at DiSs

Previous data indicate cortical DiSs are remarkably stable compared to neighboring SiSs.⁸ Thus, we tested whether DiSs

are capable of morphological plasticity using a glutamate uncaging protocol.¹⁰ Neurons were transfected with tdTom along with Geph_{FingR}-GFP. Spines with and without Geph_{FingR}-GFP signal were targeted for single-photon (rat cultures) or two-photon (2P) (mouse organotypic slices) glutamate uncaging-induced spine growth (Figure 3A and S3A). These experiments were conducted in the presence of tetrodotoxin (TTX) to avoid possible dampening of excitatory responses by coincident phasic GABA release. In both preparations, high-frequency glutamate uncaging (Glu HFU, 30 pulses at 1 Hz) elicited robust growth of SiSs (Figures 3A, 3B, and S3A). There was no relationship between the magnitude of SiS spine growth and distance to the nearest shaft inhibitory input (Figure 3C). Surprisingly, structural plasticity did not occur at DiSs in response to the same stimulus (Figures 3D, 3E, and S3A). Note that we targeted DiS and SiS groups with similar initial sizes, since the degree of plasticity-induced growth depends on initial spine size¹⁰ (Figures 3F and

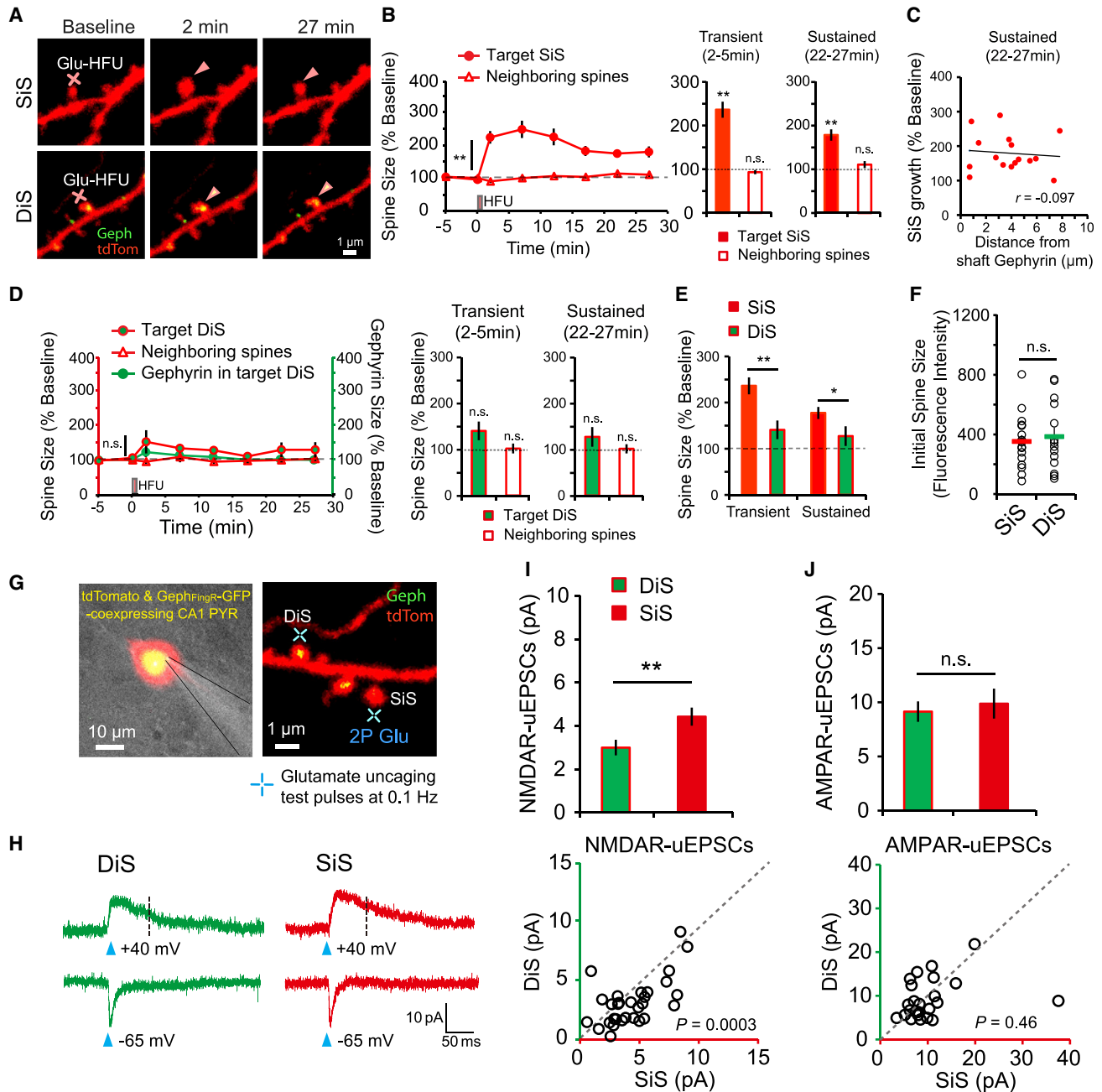


Figure 3. DiSs resist structural plasticity through attenuated NMDAR function

(A) Time-lapse images of SLM dendrites from CA1 pyramidal neurons co-expressing tdTom (red) and Geph_{FingR}-GFP (green). A SiS or DiS was exposed to high-frequency glutamate uncaging (Glu HFU) at locations indicated by the red crosses.

(B) HFU triggered robust growth of SiSs ($n = 17$ spines, 14 cells) compared with unstimulated neighboring spines ($n = 106$ spines, 14 cells). Transient (left, 2–5 min post HFU) and sustained (right, 22–27 min post HFU) increases in SiS volume (but not that of neighboring unstimulated spines) occurred following HFU. $**p < 0.01$, Student's *t* test.

(C) Growth of SiSs ($n = 16$ spines, 13 cells) is plotted as a function of distance to the nearest shaft inhibitory input. Structural plasticity was not influenced by proximity to shaft inhibitory synapses. $p = 0.729$, Pearson's correlation.

(D) Time course of DiS size or Geph_{FingR}-GFP intensity following HFU. Both transient and sustained structural plasticity were blocked at DiSs (HFU-targeted DiS: $n = 14$ spines, 13 cells; neighboring unstimulated control spines: $n = 69$ spines, 13 cells). n.s. not significant, Student's *t* test.

(E) Direct comparison between SiSs and DiSs for transient (2–5 min post HFU) and sustained (22–27 min post HFU) structural plasticity $*p < 0.05$, $**p < 0.01$, Student's *t* test.

(F) The initial size of spines targeted for plasticity was indistinguishable between SiS and DiS groups. n.s. not significant, Student's *t* test.

(legend continued on next page)

S3A). These data reveal a specific impairment of structural plasticity at DiSs.

Because structural plasticity is driven by NMDAR activation, NMDAR function at DiSs and neighboring SiSs was compared using simultaneous whole-cell patch-clamp recordings and two-photon glutamate uncaging in organotypic hippocampal slices. Uncaging-evoked NMDAR currents were reduced in amplitude at DiSs compared to nearby SiSs (Figures 3G–3I). In contrast, alpha-amino 3-hydroxy-5-methyl-4 isoxazole propionic acid receptor (AMPA) currents were comparable (Figure 3J). NMDAR-dependent Ca^{2+} entry in response to glutamate uncaging was directly monitored using the genetically encoded Ca^{2+} indicator GCaMP6s.²⁴ These experiments were performed using confocal imaging of dissociated hippocampal cultures, which also exhibit plasticity impairment selectively at DiSs, to overcome the challenges of three-color 2P uncaging/imaging (Figures S3 and S3B). We observed a significant decrease in 1P uncaging-evoked NMDAR-mediated Ca^{2+} transients at DiSs compared to neighboring SiSs (Figures S3C and S3D). To test if differences were due to NMDAR subunit composition, Ca^{2+} influx at individual spines was measured in response to either glutamate uncaging or spontaneous, quantal neurotransmitter release before and after inhibiting GluN2B-containing NMDARs with ifenprodil.²⁵ Ifenprodil blocked a similar fraction of Ca^{2+} entry at DiSs and SiSs, and Ca^{2+} entry at DiSs remained significantly impaired relative to neighboring SiSs even in the continued presence of ifenprodil (Figures S3C–S3F). Therefore, differences in Ca^{2+} entry are unlikely to arise from differences in the number or function of GluN2B-containing NMDARs.

NMDARs at DiSs are modulated by inhibitory input and GABA_BR signaling

We next investigated the origin of the inhibitory inputs onto DiSs. Somatostatin-expressing interneurons (SST-INs) preferentially innervate pyramidal cell dendrites. Thus, we infected organotypic slices from SST-Cre mice with cre-dependent (flip excision, FLEX) Sph-HT AAV to visualize SST-IN terminals. Slices were subsequently transfected with tdTom and Geph_{FingR}-GFP to identify DiSs on CA1 pyramidal neurons. Sph-HT signal was observed closely associated with DiSs (Figures S4A and S4B). To assess whether GABA release from SST-INs was responsible for reduced NMDAR function at DiSs, organotypic slices from SST-Cre mice were infected with FLEX TeNT_{LC} AAV (Figure 4A).²⁶ The efficacy of TeNT_{LC} silencing was confirmed by co-infecting slices from SST-Cre mice with high titer FLEX channelrhodopsin-2 (ChR2) AAV. Light-evoked inhibitory postsynaptic currents (IPSCs) recorded from CA1 neurons were nearly eliminated in slices infected with FLEX ChR2 and TeNT_{LC} AAVs (Figures S4C and S4D). Glutamate uncaging-evoked NMDAR currents were next measured at

DiSs and SiSs of CA1 pyramidal neurons in SST-Cre slices infected with FLEX-TeNT_{LC} AAV. With GABA release blocked from SST interneurons, DiS NMDAR currents were indistinguishable from those of neighboring SiSs (Figures 4B and 4C). Importantly, TeNT_{LC} expression in SST-interneurons did not affect NMDAR currents at SiSs (Figure 4C). Next, organotypic slices were preincubated with either GABA_AR antagonist, bicuculline, or GABA_BR antagonist, CGP55845, for varying times before measuring NMDAR function (Figures 4D and S4E). Uncaging-evoked NMDAR currents at DiSs remained significantly impaired relative to SiSs in slices treated with bicuculline (Figure S4E). However, either long-term (36–48 h; Figure S4E) or short-term (3–4hrs; Figure 4E) blockade of GABA_BRs with CGP55845 rescued NMDAR currents at DiSs to levels indistinguishable from neighboring SiSs. CGP55845 treatment did not affect NMDAR currents at SiSs or overall development or morphology of DiSs or SiSs (Figures S4E–S4H). Blocking GABA_BRs with CGP55845 for shorter times (2–12 min) was ineffective in restoring NMDAR currents or Ca^{2+} entry at DiSs (Figures 4F and S4I). Thus, reversal of the GABA_BR impact on NMDAR function at DiSs is relatively slow, taking tens of minutes to hours.

To confirm whether GABA_BR activation directly decreases NMDAR currents at DiSs, two-color, two-photon photolysis of caged glutamate and GABA was used. Natural GABAergic transmission was blocked with FLEX-TeNT_{LC} AAV using SST-Cre mice to restore NMDAR function at DiSs (Figure 4G). Repetitive 2P GABA uncaging (GABA HFU, 60 pulses at 10 Hz) significantly reduced uncaging-evoked NMDAR currents at DiSs, but not at nearby SiSs on the same dendritic segment, even though GABA_BR were observed by immunostaining at both DiSs and SiSs (Figures 4H–4J, and S4J). This effect was completely inhibited by bath application of CGP55845 (Figure 4J), further supporting a role for DiS-specific regulation of NMDAR function by GABA_BR signaling. Importantly, inhibiting GABA_BRs not only restored NMDAR function but also rescued structural plasticity of DiSs with no effect on neighboring SiSs (Figures 4K–4M). Together, these data demonstrate tonic GABA_BR signaling reduces NMDAR function and plasticity specifically at DiSs, revealing the importance of inhibitory signaling for DiS structural stability.

DISCUSSION

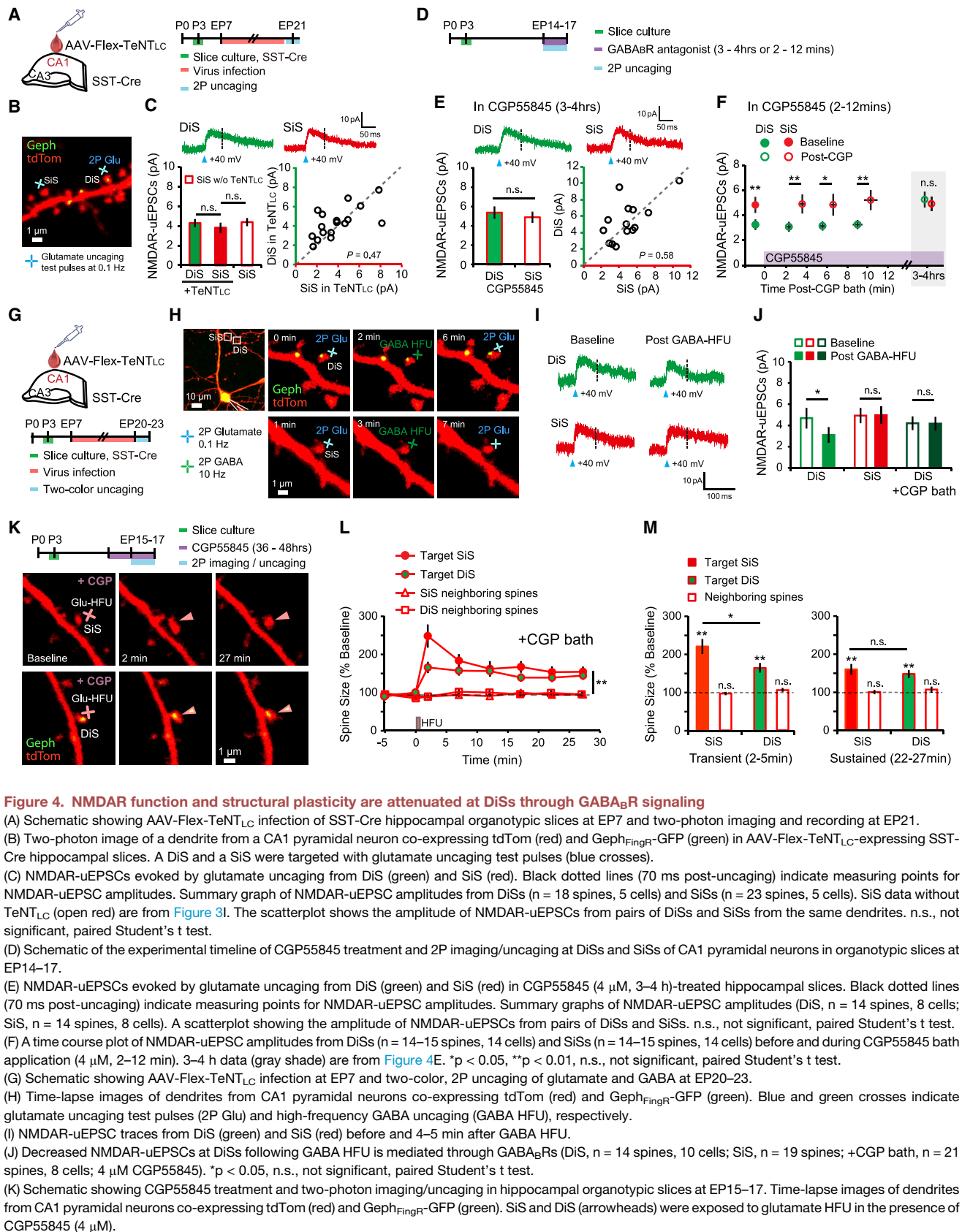
While inhibitory synaptic contacts occur directly on dendritic spines throughout the neocortex, the development and functional properties of DiSs have remained largely uncharacterized. Why does dual innervation occur to begin with? One possibility is that inhibition is recruited to mature spines in an activity-dependent manner to dampen overactive sites of excitation. For

(G) Differential interference contrast (DIC) image of an organotypic hippocampal slice culture showing a CA1 pyramidal neuron transfected with tdTom and Geph_{FingR}-GFP targeted for whole-cell recording. Blue crosses indicate two-photon glutamate uncaging spots at DiSs and SiSs on the same dendritic segment.

(H) Uncaging evoked excitatory postsynaptic currents (uEPSCs) from a DiS (green) and neighboring SiS (red) measured in whole-cell voltage-clamp mode at -65 mV for AMPARs and $+40$ mV for NMDARs. Black dotted lines (70 ms post-uncaging) indicate measuring points for NMDAR-uEPSC amplitudes.

(I) Summary graph of NMDAR-uEPSC amplitudes from DiSs ($n = 30$ spines, 11 cells) and SiSs ($n = 30$ spines, 11 cells). ** $p < 0.01$, paired Student's t test. A scatterplot is shown below for NMDAR-uEPSCs from pairs of DiSs and SiSs from the same dendrite.

(J) Summary graph of AMPAR-uEPSC amplitudes from DiSs ($n = 24$ spines, 11 cells) and SiSs ($n = 25$, 11 cells). A scatterplot showing the amplitude of AMPAR-uEPSCs from pairs of DiSs and SiSs from the same dendrite. n.s. not significant, paired Student's t test.



(legend continued on next page)

example, a recent study in cortex report that DiS excitatory PSDs are larger than SiS PSDs, suggesting the excitatory input had been potentiated.⁴ However, in hippocampus no difference was observed. Their comparable size distribution to neighboring SiSs is consistent with their resistance to potentiation and growth. In fact, DiSs in hippocampus form even when glutamate release from the associated excitatory terminal was blocked. While excitatory function may not be required for DiS development, it could play a role in subsequent DiS dynamics. For example, in the visual cortex of adult mice, the rate of gephyrin disassembly and reassembly at DiSs depends on sensory input.⁸ Whether similar dynamics occur in hippocampus and whether plasticity could occur during periods of gephyrin disassembly remain unknown.

While the inhibitory component of dual innervation most certainly plays a powerful role in dampening plasticity during coincident GABA_AR activation,^{3,13} our experiments reveal an additional layer of regulation through tonic GABA_BR signaling. This finding was surprising, since DiSs were identified based on the postsynaptic marker gephyrin, yet GABA_BRs do not appear enriched at the inhibitory postsynaptic membrane.²⁷ Previous studies demonstrate potent GABA_BR regulation of NMDAR function.^{12,14} However, these studies relied on global pharmacological activation of GABA_BRs, leaving it unclear precisely where this regulation naturally occurs and what its functional consequences are. We found that NMDARs are suppressed specifically at DiSs, and this regulation is sufficient to impair structural plasticity. While GABA_BRs may be broadly distributed, our GABA uncaging data indicate that they play a selective role in regulating NMDAR function at DiSs, perhaps due to select localization of specific GABA_BR isoforms and/or activation of downstream signaling molecules only present at DiSs.^{28,29} Their proximity to the excitatory PSD, along with spatial boundaries imposed by the spine membrane, result in highly localized crosstalk signaling sufficient to impair nearby NMDARs and structural plasticity without influencing neighboring SiSs. More experiments are needed to delineate the downstream mechanisms, but previous studies using global pharmacological activation of GABA_BRs reported reduced NMDAR-mediated Ca²⁺ entry, but not total current, through regulation of a phosphorylation site on GluN2B.^{14,30} However, the GABA_BR-dependent regulation of NMDARs that we observed in hippocampus appears distinct. First, we observed that both Ca²⁺ entry and overall current were reduced at DiSs compared to neighboring SiSs. Furthermore, selectively blocking GluN2B-containing NMDA receptors reduced Ca²⁺ entry to a similar extent at both DiSs and SiSs and did not normalize their respective Ca²⁺ responses. Instead, NMDAR function could be regulated through a distinct signaling mechanism. Multiple kinase pathways can regulate NMDAR channel properties, clustering, and localization through direct phosphorylation or indirect mechanisms.^{31–33}

While the role of DiSs in circuit function remains unclear, previous longitudinal *in vivo* imaging studies in cortex demonstrate

DiSs are much less dynamic in shape and size compared to SiSs, suggesting they could act as stable points of circuit connectivity in the face of ongoing plasticity and turnover at neighboring singly innervated inputs.^{7,8} A subset of immutable synaptic connections could maintain a stable thread of circuit connectivity, which may be especially important in brain regions with high synapse turnover and plasticity. Indeed, complete turnover of dendritic spines could take place within weeks on CA1 hippocampal pyramidal neurons.³⁴ The relatively slow reversal of NMDAR impairment at DiSs upon GABA_BR antagonism suggests these synapses are unlikely to revert to a plastic state during brief pauses in GABA release, contributing to their long-term stability.

STAR★METHODS

Detailed methods are provided in the online version of this paper and include the following:

- KEY RESOURCES TABLE
- RESOURCE AVAILABILITY
 - Lead contact
 - Materials availability
 - Data and code availability
- EXPERIMENTAL MODEL AND SUBJECT DETAILS
- METHOD DETAILS
 - 3D reconstruction from serial section electron microscopy
 - *In utero* electroporation, perfusion, and slice preparation
 - Organotypic and dissociated culture preparation
 - Adeno-associated virus preparation
 - Confocal Ca²⁺ imaging and 1-photon MNI-glutamate uncaging
 - FM dye loading
 - Electrophysiology
 - Two-photon imaging and high-frequency glutamate uncaging
 - Optogenetic IPSCs
 - Pharmacology
- QUANTIFICATION AND STATISTICAL ANALYSES
 - Image analysis and quantification
 - Uncaging evoked IPSCs and EPSCs
 - Optogenetically evoked IPSCs
 - Statistical analyses

SUPPLEMENTAL INFORMATION

Supplemental information can be found online at <https://doi.org/10.1016/j.neuron.2022.11.002>.

ACKNOWLEDGMENTS

We thank Mark Dell'Acqua and Christopher Ford for critical discussions; Jonathan E. Tullis for script development; Hannah Actor-Engel for 3D

(L) HFU increased the volume of SiSs (n = 12 spines, 11 cells) and DiSs (n = 13 spines, 10 cells) compared with unstimulated neighboring spines (SiS neighbors, n = 79 spines, 11 cells; DiS neighbors, n = 65 spines, 10 cells) in the presence of CGP55845. **p < 0.01, Student's t test.

(M) HFU increased both transient (left, changes over 2–5 min) and sustained (right, changes over 22–27 min) volume of SiS and DiS, but not unstimulated spines, compared with baseline in CGP55845. **p < 0.01, *p < 0.05, n.s. not significant, Student's t test.

reconstructions; John Mendenhall, Clayton Smith, Libby Perry, and Robert Smith for preparation of 3DEM data sets; and Jennifer Bourne, Michael Chirillo, Katherine Dembny, Corey Haines, Alyssa Herbot, Matthew Hooper, Zean Luna, Jordan Mackey, Patrick Parker, and Kyle Zatyko for manual tracing 3DEM datasets. Funding sources include NIGMS T32GM007635 (D.J.K.); NIA F32 AG071073 (O.P.); NINDS R35NS116879, UF1NS107710, NS110383 (M.J.K.), and T32NS099042 (R.O.); NICHD F31HD106632 (R.O.); NIMH R01MH124778, R21MH126073 (W.C.O.), and 5R56MH095980-07 (K.M.H.); Brain and Behavioral Research Foundation (W.C.O.); Brain Research Foundation (W.C.O.); CSU/CU-Pilot Collaboration Award (W.C.O.); National Center for Advancing Translational Sciences UL1TR002535; Boettcher Foundation and Children's Hospital Colorado Program in Pediatric Stem Cell Biology (S.J.F.); and NSF 1707356 and 2014862 (K.M.H.).

AUTHOR CONTRIBUTIONS

Conceptualization, M.J.K., W.C.O.; investigation/data analysis, W.C.A., W.C.B., S.J.F., D.D.H., D.J.K., I.-W.H., M.K., M.J.K., M.S.K., R.O., S.L.O., S.J.F., W.C.O., O.P., L.E.G.W.; writing – original draft, K.M.H., M.K., M.J.K., M.S.K., W.C.O.; writing – review and editing, W.C.A., K.M.H., M.J.K., M.S.K., M.K., W.C.O.; funding acquisition, S.J.F., K.M.H., M.J.K., M.S.K., W.C.O.; supervision, K.M.H., M.J.K., W.C.O.

DECLARATION OF INTERESTS

The authors declare no competing interests.

INCLUSION AND DIVERSITY

We support inclusive, diverse, and equitable conduct of research.

Received: December 13, 2021

Revised: July 13, 2022

Accepted: October 31, 2022

Published: November 16, 2022

REFERENCES

1. Kubota, Y., Hatada, S., Kondo, S., Karube, F., and Kawaguchi, Y. (2007). Neocortical inhibitory terminals innervate dendritic spines targeted by thalamocortical afferents. *J. Neurosci. : the official journal of the Society for Neuroscience* 27, 1139–1150. <https://doi.org/10.1523/JNEUROSCI.3846-06.2007>.
2. Wilson, C.J., Groves, P.M., Kitai, S.T., and Linder, J.C. (1983). Three-dimensional structure of dendritic spines in the rat neostriatum. *J. Neurosci. : the official journal of the Society for Neuroscience* 3, 383–388. <https://doi.org/10.1523/jneurosci.03-02-00383.1983>.
3. Chiu, C.Q., Lur, G., Morse, T.M., Carnevale, N.T., Ellis-Davies, G.C.R., and Higley, M.J. (2013). Compartmentalization of GABAergic inhibition by dendritic spines. *Science (New York, N.Y.)* 340, 759–762. <https://doi.org/10.1126/science.1234274>.
4. Gemin, O., Serna, P., Zamith, J., Assendorp, N., Fossati, M., Rostaing, P., Triller, A., and Charrier, C. (2021). Unique properties of dually innervated dendritic spines in pyramidal neurons of the somatosensory cortex uncovered by 3D correlative light and electron microscopy. *PLoS Biol.* 19, e3001375. <https://doi.org/10.1371/journal.pbio.3001375>.
5. Iascone, D.M., Li, Y., Sümbül, U., Doron, M., Chen, H., Andreu, V., Goudy, F., Blockus, H., Abbott, L.F., Segev, I., et al. (2020). Whole-Neuron Synaptic Mapping Reveals Spatially Precise Excitatory/Inhibitory Balance Limiting Dendritic and Somatic Spiking. *Neuron* 106, 566–578. e8. <https://doi.org/10.1016/j.neuron.2020.02.015>.
6. Isshiki, M., Tanaka, S., Kuriu, T., Tabuchi, K., Takumi, T., and Okabe, S. (2014). Enhanced synapse remodeling as a common phenotype in mouse models of autism. *Nat. Commun.* 5, 4742. <https://doi.org/10.1038/ncomms5742>.
7. Chen, J., Villa, K., Cha, J., So, P., Kubota, Y., and Nedivi, E. (2012). Clustered dynamics of inhibitory synapses and dendritic spines in the adult neocortex. *Neuron* 74, 361–373. <https://doi.org/10.1016/j.neuron.2012.02.030>.
8. Villa, K.L., Berry, K.P., Subramanian, J., Cha, J.W., Oh, W.C., Kwon, H.-B., Kubota, Y., So, P.T., and Nedivi, E. (2016). Inhibitory Synapses Are Repeatedly Assembled and Removed at Persistent Sites *In Vivo*. *Neuron* 89, 756–769. <https://doi.org/10.1016/j.neuron.2016.01.010>.
9. Knott, G.W., Quairiaux, C., Genoud, C., and Welker, E. (2002). Formation of dendritic spines with GABAergic synapses induced by whisker stimulation in adult mice. *Neuron* 34, 265–273. [https://doi.org/10.1016/s0896-6273\(02\)00663-3](https://doi.org/10.1016/s0896-6273(02)00663-3).
10. Matsuzaki, M., Honkura, N., Ellis-Davies, G.C.R., and Kasai, H. (2004). Structural basis of long-term potentiation in single dendritic spines. *Nature* 429, 761–766. <https://doi.org/10.1038/nature02617>.
11. Yang, Y., Wang, X.B., Frerking, M., and Zhou, Q. (2008). Spine expansion and stabilization associated with long-term potentiation. *J. Neurosci.* 28, 5740–5751. <https://doi.org/10.1523/jneurosci.3998-07.2008>.
12. Chalifoux, J.R., and Carter, A.G. (2010). GABAB receptors modulate NMDA receptor calcium signals in dendritic spines. *Neuron* 66, 101–113.
13. Hayama, T., Noguchi, J., Watanabe, S., Takahashi, N., Hayashi-Takagi, A., Ellis-Davies, G.C.R., Matsuzaki, M., and Kasai, H. (2013). GABA promotes the competitive selection of dendritic spines by controlling local Ca²⁺ signaling. *Nat. Neurosci.* 16, 1409–1416. <https://doi.org/10.1038/nn.3496>.
14. Lur, G., and Higley, M. (2015). Glutamate Receptor Modulation Is Restricted to Synaptic Microdomains. *Cell Rep.* 12, 326–334. <https://doi.org/10.1016/j.celrep.2015.06.029>.
15. Gross, G., Junge, J., Mora, R., Kwon, H.-B., Olson, C., Takahashi, T., Liman, E., Ellis-Davies, G., McGee, A., Sabatini, B., et al. (2013). Recombinant probes for visualizing endogenous synaptic proteins in living neurons. *Neuron* 78, 971–985. <https://doi.org/10.1016/j.neuron.2013.04.017>.
16. Grimm, J.B., English, B.P., Chen, J., Slaughter, J.P., Zhang, Z., Revyakin, A., Patel, R., Macklin, J.J., Normanno, D., Singer, R.H., et al. (2015). A general method to improve fluorophores for live-cell and single-molecule microscopy. *Nat. Methods* 12, 244–250. <https://doi.org/10.1038/nmeth.3256>.
17. Hazan, L., and Ziv, N.E. (2020). Activity dependent and independent determinants of synaptic size diversity. *J. Neurosci.* 40, 2828–2848. <https://doi.org/10.1523/JNEUROSCI.2181-19.2020>.
18. Lee, M.C., Yasuda, R., and Ehlers, M.D. (2010). Metaplasticity at single glutamatergic synapses. *Neuron* 66, 859–870. <https://doi.org/10.1016/j.neuron.2010.05.015>.
19. Liu, Q., Sinnen, B.L., Boxer, E.E., Schneider, M.W., Grybko, M.J., Buchta, W.C., Gibson, E.S., Wysoczynski, C.L., Ford, C.P., Gottschalk, A., et al. (2019). A Photoactivatable Botulinum Neurotoxin for Inducible Control of Neurotransmission. *Neuron* 101, 863–875.e6. <https://doi.org/10.1016/j.neuron.2019.01.002>.
20. Sando, R., Bushong, E., Zhu, Y., Huang, M., Considine, C., Phan, S., Ju, S., Uytiepo, M., Ellisman, M., and Maximov, A. (2017). Assembly of Excitatory Synapses in the Absence of Glutamatergic Neurotransmission. *Neuron* 94, 312–321.e3. <https://doi.org/10.1016/j.neuron.2017.03.047>.
21. Sigler, A., Oh, W.C., Imig, C., Altas, B., Kawabe, H., Cooper, B.H., Kwon, H.-B., Rhee, J.-S., and Brose, N. (2017). Formation and Maintenance of Functional Spines in the Absence of Presynaptic Glutamate Release. *Neuron* 94, 304–311.e4. <https://doi.org/10.1016/j.neuron.2017.03.029>.
22. Zhu, Y., Uytiepo, M., Bushong, E., Haberl, M., Beutter, E., Scheiwe, F., Zhang, W., Chang, L., Luu, D., Chui, B., et al. (2021). Nanoscale 3D EM reconstructions reveal intrinsic mechanisms of structural diversity of chemical synapses. *Cell Rep.* 35, 108953. <https://doi.org/10.1016/j.celrep.2021.108953>.
23. Choi, J.-H., Sim, S.-E., Kim, J.-I., Choi, D.I., Oh, J., Ye, S., Lee, J., Kim, T., Ko, H.-G., Lim, C.-S., and Kaang, B.-K. (2018). Interregional synaptic maps among engram cells underlie memory formation. *Science (New York, N.Y.)* 360, 430–435. <https://doi.org/10.1126/science.aas9204>.

24. Chen, T.-W., Wardill, T.J., Sun, Y., Pulver, S.R., Renninger, S.L., Baohan, A., Schreiter, E.R., Kerr, R.A., Orger, M.B., Jayaraman, V., et al. (2013). Ultrasensitive fluorescent proteins for imaging neuronal activity. *Nature* 499, 295–300. <https://doi.org/10.1038/nature12354>.
25. Sinnen, B.L., Bowen, A.B., Gibson, E.S., and Kennedy, M.J. (2016). Local and use-dependent effects of β -Amyloid oligomers on NMDA receptor function revealed by optical quantal analysis. *J. Neurosci.* 36, 11532–11543. <https://doi.org/10.1523/JNEUROSCI.1603-16.2016>.
26. Oh, W.C., Lutz, S., Castillo, P.E., and Kwon, H.-B. (2016). De novo synaptogenesis induced by GABA in the developing mouse cortex. *Science* (New York, N.Y.) 353, 1037–1040. <https://doi.org/10.1126/science.aaf5206>.
27. Kulik, A., Vida, I., Luján, R., Haas, C.A., López-Bendito, G., Shigemoto, R., and Frotscher, M. (2003). Subcellular localization of metabotropic GABA(B) receptor subunits GABA(B1a/b) and GABA(B2) in the rat hippocampus. *J. Neurosci. : the official journal of the Society for Neuroscience* 23, 11026–11035. 2003. <https://doi.org/10.1523/jneurosci.23-35-11026.2003>.
28. Bettler, B., Kaupmann, K., Mosbacher, J., and Gassmann, M. (2004). Molecular structure and physiological functions of GABA(B) receptors. *Physiol. Rev.* 84, 835–867. <https://doi.org/10.1152/physrev.00036.2003>.
29. Xu, C., Zhang, W., Rondard, P., Pin, J.P., and Liu, J. (2014). Complex GABAB receptor complexes: how to generate multiple functionally distinct units from a single receptor. *Front. Pharmacol.* 5, 12. <https://doi.org/10.3389/fphar.2014.00012>.
30. Murphy, J.A., Stein, I.S., Lau, C.G., Peixoto, R.T., Aman, T.K., Kaneko, N., Aromolaran, K., Saulnier, J.L., Popescu, G.K., Sabatini, B.L., et al. (2014). Phosphorylation of Ser1166 on GluN2B by PKA Is Critical to Synaptic NMDA Receptor Function and Ca²⁺ Signaling in Spines. *J. Neurosci.* 34, 869–879. <https://doi.org/10.1523/JNEUROSCI.4538-13.2014>.
31. Tingley, W.G., Ehlers, M.D., Kameyama, K., Doherty, C., Ptak, J.B., Riley, C.T., and Huganir, R.L. (1997). Characterization of protein kinase A and protein kinase C phosphorylation of the N-methyl-D-aspartate receptor NR1 subunit using phosphorylation site-specific antibodies. *J. Biol. Chem.* 272, 5157–5166. <https://doi.org/10.1074/jbc.272.8.5157>.
32. Lin, Y., Jover-Mengual, T., Wong, J., Bennett, M.V.L., and Zukin, R.S. (2006). PSD-95 and PKC converge in regulating NMDA receptor trafficking and gating. *Proc. Natl. Acad. Sci. USA.* 103, 19902–19907. <https://doi.org/10.1073/pnas.0609924104>.
33. Zheng, X., Zhang, L., Wang, A.P., Bennett, M.V.L., and Zukin, R.S. (1999). Protein kinase C potentiation of N-methyl-D-aspartate receptor activity is not mediated by phosphorylation of N-methyl-D-aspartate receptor subunits. *Proc. Natl. Acad. Sci. USA.* 96, 15262–15267. <https://doi.org/10.1073/pnas.96.26.15262>.
34. Attardo, A., Fitzgerald, J.E., and Schnitzer, M.J. (2015). Impermanence of dendritic spines in live adult CA1 hippocampus. *Nature* 523, 592–596. <https://doi.org/10.1038/nature14467>.
35. Fiala, J.C. (2005). Reconstruct: a free editor for serial section microscopy. *J. Microsc.* 218, 52–61. <https://doi.org/10.1111/j.1365-2818.2005.01466.x>.
36. Schindelin, J., Arganda-Carreras, I., Frise, E., Kaynig, V., Longair, M., Pietzsch, T., Preibisch, S., Rueden, C., Saalfeld, S., Schmid, B., et al. (2012). Fiji: an open-source platform for biological-image analysis. *Nat. Methods* 9, 676–682. <https://doi.org/10.1038/nmeth.2019>.
37. Cardona, A., Saalfeld, S., Schindelin, J., Arganda-Carreras, I., Preibisch, S., Longair, M., Tomancak, P., Hartenstein, V., and Douglas, R.J. (2012). TrakEM2 Software for Neural Circuit Reconstruction. *PLoS One* 7, e38011. <https://doi.org/10.1371/journal.pone.0038011>.
38. Bowden, J.B., Abraham, W.C., and Harris, K.M. (2012). Differential effects of strain, circadian cycle, and stimulation pattern on LTP and concurrent LTD in the dentate gyrus of freely moving rats. *Hippocampus* 22, 1363–1370. <https://doi.org/10.1002/hipo.20972>.
39. Bromer, C., Bartol, T.M., Bowden, J.B., Hubbard, D.D., Hanka, D.C., Gonzalez, P.V., Kuwajima, M., Mendenhall, J.M., Parker, P.H., Abraham, W.C., et al. (2018). Long-term potentiation expands information content of hippocampal dentate gyrus synapses. *Proceedings of the National Academy of Sciences of the United States of America* 115, E2410–E2418. <https://doi.org/10.1073/pnas.1716189115>.
40. Bourne, J.N., and Harris, K.M. (2011). Coordination of size and number of excitatory and inhibitory synapses results in a balanced structural plasticity along mature hippocampal CA1 dendrites during LTP. *Hippocampus* 21, 354–373. <https://doi.org/10.1002/hipo.20768>.
41. Jensen, F.E., and Harris, K.M. (1989). Preservation of neuronal ultrastructure in hippocampal slices using rapid microwave-enhanced fixation. *J. Neurosci. Methods* 29, 217–230. [https://doi.org/10.1016/0165-0270\(89\)90146-5](https://doi.org/10.1016/0165-0270(89)90146-5).
42. Reynolds, E.S. (1963). THE USE OF LEAD CITRATE AT HIGH pH AS AN ELECTRON-OPAQUE STAIN IN ELECTRON MICROSCOPY. *JCB (J. Cell Biol.)* 17, 208–212. <https://doi.org/10.1083/jcb.17.1.208>.
43. Kuwajima, M., Mendenhall, J.M., Lindsey, L.F., and Harris, K.M. (2013). Automated Transmission-Mode Scanning Electron Microscopy (tSEM) for Large Volume Analysis at Nanoscale Resolution. *PLoS One* 8, e59573. <https://doi.org/10.1371/journal.pone.0059573>.
44. Saalfeld, S., Fetter, R., Cardona, A., and Tomancak, P. (2012). Elastic volume reconstruction from series of ultra-thin microscopy sections. *Nat. Methods* 9, 717–720. <https://doi.org/10.1038/nmeth.2072>.
45. Fiala, J.C., and Harris, K.M. (2001). Cylindrical diameters method for calibrating section thickness in serial electron microscopy. *J. Microsc.* 202, 468–472. <https://doi.org/10.1046/j.1365-2818.2001.00926.x>.
46. Stoppini, L., Buchs, P.A., and Muller, D. (1991). A simple method for organotypic cultures of nervous tissue. *J. Neurosci. Methods* 37, 173–182. [https://doi.org/10.1016/0165-0270\(91\)90128-M](https://doi.org/10.1016/0165-0270(91)90128-M).
47. Woods, G., and Zito, K. (2008). Preparation of gene gun bullets and biolistic transfection of neurons in slice culture. *JoVE : JoVE* 10, 675. <https://doi.org/10.3791/675>.
48. Aoto, J., Martinelli, D., Malenka, R., Tabuchi, K., and Südhof, T. (2013). Presynaptic neurexin-3 alternative splicing trans-synaptically controls postsynaptic AMPA receptor trafficking. *Cell* 154, 75–88. <https://doi.org/10.1016/j.cell.2013.05.060>.
49. Kim, J., Lee, S., Jung, K., Oh, W.C., Kim, N., Son, S., Jo, Y., Kwon, H.-B., and Heo, W.D. (2019). Intensiometric biosensors visualize the activity of multiple small GTPases in vivo. *Nat. Commun.* 10, 211. <https://doi.org/10.1038/s41467-018-08217-3>.

STAR★METHODS

KEY RESOURCES TABLE

REAGENT or RESOURCE	SOURCE	IDENTIFIER
Antibodies		
Guinea pig polyclonal anti-vGAT	Synaptic Systems	Cat #131004; RRID:AB_887873
Mouse monoclonal anti-Synaptobrevin 2 (Vamp2)	Synaptic Systems	Cat #; 104,211 RRID:AB_2619758
Guinea pig polyclonal anti-GABA _A R γ 2	Synaptic Systems	Cat #; 224,004 RRID:AB_10594245
Mouse monoclonal anti GABA _B receptor	Neuromab	Cat #N39A/49
Goat anti-Mouse IgG H&L Alexa Fluor 647	Invitrogen	Cat #; A-21236 RRID:AB_2535805
Goat anti-Guinea pig IgG H&L Alexa Fluor 647	Abcam	Cat #; ab150187 RRID:AB_2827756
Goat anti-Guinea pig IgG H&L Alexa Fluor 405	Abcam	Cat #; ab175678 RRID:AB_2827755
Bacterial and virus strains		
AAV DJ-Sph-HT-T2A-TeNT _{LC}	This paper	N/A
AAV DJ-Flex-Sph-HT	This paper	N/A
AAV DJ-eGRASP _{pre} -T2A-TeNT _{LC}	This paper	N/A
AAV 1-EF1-dflox-hChr2(h134R)-mCherry-WPRE-hGH	Gift from Karl Deisseroth	Addgene Viral prep #20297-AAV1
AAV DJ-Flex-TeNT _{LC}	Oh, W.C. et al. ²⁶	N/A
Chemicals, peptides, and recombinant proteins		
JF646-Halotag ligand	HHMI Janelia Materials	https://janeliamaterials.azurewebsites.net/
Ifenprodil	Tocris Bioscience	#0545
CGP55845	Tocris Bioscience	#1248
Tetrodotoxin citrate	Tocris Bioscience	#1069
(R)-CPP	Tocris Bioscience	#0247
Bicuculline methochloride	Tocris Bioscience	#2503
NBQX disodium salt	Tocris Bioscience	#0373
DL-AP5 sodium salt	Tocris Bioscience	#3693
Advasep-7	Sigma	#A3723
MNI-glutamate	Tocris Bioscience	#1490
RuBi-GABA	Tocris Bioscience	#3574
FM4-64	Molecular Probes/Thermo	Invitrogen #F34653
Experimental models: Organisms/strains		
Mouse: C57BL/6J	Jackson Laboratory	Strain 000,664 RRID:IMSR_JAX:000,664
Mouse: Somatostatin-Cre	Jackson Laboratory	Sst-IRES-Cre, strain 13,044 RRID:IMSR_JAX:013,044
Rat: Sprague Dawley	Charles River	Cr1:CD(SD)BR; RRID: RGD_734476
Mouse: CD-1 IGS	Charles River	Cr1:CD1(ICR) Strain Code 022
Recombinant DNA		
pGP-CMV-GCaMP6s	Chen et al. ²⁴	Addgene Cat #40753
PSD95-FingR-GFP	Gross et al. ¹⁵	Addgene Cat #46295
Gephyrin-FingR-mScarlet	This paper	N/A
HaloTag-pDisplay	This paper	N/A
EWB-DIO-myrTagRFP-T-P2A-post-eGRASP	Choi et al. ²³	Addgene Cat #111581
Gephyrin-FingR-GFP	Gross et al. ¹⁵	Addgene Cat #46296
FCtdT-Cre	This paper	N/A

(Continued on next page)

Continued

REAGENT or RESOURCE	SOURCE	IDENTIFIER
Software and algorithms		
Reconstruct Software	Fiala, J.C. ³⁵	https://synapseweb.clm.utexas.edu/software-0
Fiji	Schindelin, J. et al. ³⁶	RRID:SCR_002285
Metamorph	Molecular Devices	https://www.moleculardevices.com/systems/metamorph-research-imaging/metamorph-microscopy-automation-and-image-analysis-software
ImageJ	National Institute of Health	https://imagej.nih.gov/ij/
DualSynapse analysis software	This paper	https://github.com/mjkennedylab/DualSynapse
TrakEM2	Cardona, A. et al. ³⁷	RRID:SCR_008954
GraphPad Prism	http://www.graphpad.com	Prism Version 9.0.1
Clampfit 10.3	Molecular Devices	https://www.moleculardevices.com/
OriginPro 8.5	OriginLab	https://www.originlab.com/
Open Broadcaster Software	OBS Studio Contributors	https://obsproject.com
Other		
1.6 μ m gold particles	Biorad	#1652264

RESOURCE AVAILABILITY

Lead contact

Requests for materials and reagents related to this study will be fulfilled by the lead contact, Matthew J. Kennedy (matthew.kennedy@cuanschultz.edu).

Materials availability

Plasmids generated in this study will be made available through Addgene plasmid repository. Until Addgene catalog numbers are assigned, plasmids will be made available upon request without restriction.

Data and code availability

- All data necessary to assess the conclusions of this work are available in the text and supplemental materials. Any additional information or raw data files are available from the lead contact upon request.
- Original ImageJ code for automating dually-innervated spine detections has been deposited at: <https://github.com/mjkennedylab/DualSynapse>.
- Any additional information required to reanalyze the data reported in this paper is available from the lead contact upon request.

EXPERIMENTAL MODEL AND SUBJECT DETAILS

We used wild-type and C57BL/6 mice (Jackson Laboratory), somatostatin-Cre mice (Jackson Laboratory, Sst-IRES-Cre 13,044) and Sprague-Dawley rats (Charles River). Mice were used at postnatal day 5–7 (organotypic slices) or 13–25 (perfusion fixed brains). In all experiments, data were obtained from both male and female animals in equal proportions. No influence from sex was determined. All animals were group-housed with free access to food/water in accordance with the University of Colorado Institutional Animal Care and Use Committee. 3-dimensional electron microscopy reconstructions and quantifications were performed on tissue samples prepared for previously published studies using Long-Evans rats (60–170 days old).^{38,39}

METHOD DETAILS

3D reconstruction from serial section electron microscopy

Animals. All animal procedures for 3DEM were performed in accordance with the Guide for the Care and Use of Laboratory Animals of the National Institutes of Health. The animal protocols were approved by animal care and use committees at Children's Hospital (Boston, MA), Medical College of Georgia (Augusta, GA), The University of Texas at Austin, or the Otago University Animal Ethics Committee.

All 3DEM data were collected from adult male Long-Evans rats (Charles River or Animal Breeding Station at the University of Otago). We prepared two acute hippocampal slices from two rats aged 60–61 days old that were anesthetized with halothane and decapitated. The slices (400 μm thickness) were collected from the middle third of the hippocampus and recovered in an interface chamber in artificial cerebrospinal fluid for electrophysiology recordings to induce long-term potentiation (LTP) at Schaffer collateral synapses in area CA1 as described previously.⁴⁰ Hippocampal slices were fixed within 1 min of the last recording in fixative (6% glutaraldehyde and 2% paraformaldehyde in 0.1 M sodium cacodylate buffer with 2 mM CaCl_2 and 4 mM MgSO_4), enhanced by microwave irradiation for 10 s.⁴¹ We obtained and analyzed four 3DEM datasets (two control and two LTP) from these slices. Another SR dataset was collected from a rat (68 days old) that was perfusion-fixed transcardially with the same fixative under pentobarbital anesthesia. Three 3DEM datasets were obtained from SLM of two rats that were perfusion-fixed under halothane anesthesia with 2.5% glutaraldehyde and 2% formaldehyde in 0.1 M sodium cacodylate buffer with 2 mM CaCl_2 and 4 mM MgSO_4 . One of the two animals (170 days old) underwent *in vivo* electrophysiology recordings to induce long-term potentiation in the middle molecular layer of the hippocampal dentate gyrus in one hemisphere, as described previously.^{38,39} From this animal, we used a dataset obtained from SLM of the control hemisphere that received only test pulses delivered to medial perforant path and did not exhibit long-term plasticity. The remaining animal (162 days old) did not undergo any prior experiments and was used to generate two SLM datasets.

Tissue processing and serial sectioning. After vibratome sectioning to 70 μm thickness, the fixed tissue containing the regions of interest underwent staining with reduced osmium (1.5% $\text{K}_4\text{Fe}(\text{CN})_6$ and 1% OsO_4 in 0.1 M sodium cacodylate buffer), followed by 1% OsO_4 in the same buffer. The tissue was then stained *en bloc* with 1% uranyl acetate and dehydrated in a series of ethanol and propylene oxide, or in acetone. The dehydrated tissue was infiltrated with and embedded into LX-112 resin or mixture of Epon and Spurr's resin. The resin blocks containing the tissue were trimmed to regions of interest in area CA1. Serial ultrathin sections were cut with a diamond knife (DIATOME Ultra35 or Ultra45) on an ultramicrotome and collected on Synpatek slot grids coated with Piolo-form or polyetherimide substrate. Sections were stained with uranyl acetate, followed by lead citrate⁴² for 5 min each.

EM imaging and alignment. The serial ultrathin sections from SR were imaged, blind as to condition, with a JEOL JEM-1230 transmission electron microscope (TEM) with a Gatan UltraScan4000 CCD camera at 5,000 \times magnification. Serial section series from SLM were imaged with a transmission-mode scanning electron microscope⁴³ (tSEM; Zeiss Supra40) at 1.8–2.0 nm/pixel. A diffraction grating replica (Ernest Fullam, Inc., Latham, NY or Electron Microscopy Sciences, Hatfield, PA) was imaged along with the serial section series to calibrate pixel size.

SR dataset from the perfusion-fixed rat was imaged as two-tile mosaics, which were then stitched using Adobe Photoshop. All SR datasets were imported into and aligned with the Reconstruct software³⁵ (RRID:SCR_002716; <https://synapseweb.clm.utexas.edu/software-0>). SLM datasets were aligned first using Fiji with the TrakEM2 plugin^{36,37,44} (RRID:SCR_002285; RRID:SCR_008954; <http://fiji.sc>, <http://www.ini.uzh.ch/~acardona/trakem2.html>) and then imported into Reconstruct for analysis. Mean section thickness was calculated for each serial section series using the cylindrical diameters method by dividing the diameters of longitudinally sectioned mitochondria by the number of sections they spanned.⁴⁵

Unbiased reconstructions and statistical analyses. 3DEM datasets were given a five-letter code to mask the identity of experimental conditions in subsequent analyses. We used the Reconstruct software to identify and trace manually dendrites and synapses in the 3DEM datasets. Dendrites were sampled from SR and SLM based on microtubule count. We analyzed 31 oblique dendrites from SR containing 9–48 microtubules and ranging 1.83–21.41 μm in length. From SLM, we analyzed 36 dendrites with 6–48 microtubules and 6.34–21.01 μm in length. Putative inhibitory axons contacting dendritic spines were confirmed by tracing them to another symmetric synapse along the same axon. Of the 67 dendrites analyzed, 6 in SR and 12 in SLM contained one or more DiSs and 39 of 48 symmetric synapses in SR and 102 of 122 in SLM were located on dendritic shafts.

Statistical analyses were performed with GraphPad Prism, with statistical significance set at $p < 0.05$. We checked data for normality with Kolmogorov-Smirnov test and found only the size of symmetric synapses in SLM to be consistent with normal distribution. Thus, we used unpaired two-tailed t test to compare DiS and shaft in this layer (Figure S1B, SLM - symmetric). Synapse sizes in other categories were not distributed normally, so we used Kruskal-Wallis test for asymmetric synapses in SR and SLM, and Mann-Whitney test for symmetric synapses in SR (Figures S1A and S1B). We pooled together the dendrite and synapse size data from all conditions in SR (i.e., control, LTP, and perfusion-fixed) since DiSs were rare in this layer in adult rat CA1.

Figures and supplemental movie. For 3DEM data in Figure 1, graphs were generated with Microsoft Excel or GraphPad Prism. 3D reconstructions of the traced objects were generated as Boissonnat surface in Reconstruct. Adobe Photoshop was used to adjust brightness and contrast, and in some cases sharpness, of EM images. Adobe Illustrator was used to assemble all figures.

Rotating 3D scenes of reconstructed objects (dendrites, spines, synapses, and presynaptic axons) were rendered in Reconstruct, and screen recordings were made using Open Broadcaster Software (OBS). Recorded clips were then edited together and captions were added using Adobe Premiere.

In utero electroporation, perfusion, and slice preparation

All animal procedures were carried out in accordance with a protocol approved by the University of Colorado Denver Institutional Animal Care and Use Committee. Timed pregnant CD-1 IGS mice were ordered from Charles River (Strain Code 022). On gestation day 15.5, pregnant mice were anesthetized with vaporized isoflurane and administered analgesia (subcutaneous injection of meloxicam, 2 mg/kg). A small vertical midline incision was made in the skin and peritoneum, approximately 1.5–2.5 cm in length, to expose

the uterine horns. Beveled glass micropipettes were used to inject 1–2 μL of endotoxin-free plasmid DNA into the embryos' lateral ventricles at 1 mg/mL each. For electroporation, 5 pulses separated by 950 ms were applied at 45 V, using tweezer-type electrodes connected to a square-wave electroporator (BTX ECM 830). Electrodes were oriented to direct the current toward the midline to target the hippocampal primordium. Embryos were placed back in the dam and the peritoneal and skin incisions were closed with sterile, single-use sutures (6-0 thread size with P-1 Reverse Cutting needle). Embryos were allowed to develop *in utero* and postnatally until the indicated ages. At the indicated ages postnatal mice were anesthetized with vaporized isoflurane and transcardially perfused with 4% PFA with additional post fix in 4% PFA overnight at 4°C. Brains were cryoprotected in 30% sucrose at 4°C overnight and sectioned on a cryostat at 20 μm .

Organotypic and dissociated culture preparation

Organotypic cultures and dissociated neurons were prepared from Sprague-Dawley rats or mice as previously described.⁴⁶ Dissociated hippocampal neurons were prepared from P0-P1 pups. Dissociated hippocampal neurons were transfected between 14 and 18 days *in vitro* (DIV) with lipofectamine 2000 according to the manufacturer's protocol. Organotypic cultures, prepared from P5-P7 rats or P2-P3 mice, were cultured for 7–18 days before biolistic transfection with plasmids encoding synaptic/morphology markers. Subsequent imaging/uncaging/whole cell patch clamp recordings were performed within 24–50 h following biolistic transfection (between 9 and 18 days *in vitro*). Biolistic transfection and gold particle preparation was carried out as previously described.⁴⁷ In some cases, slices were infected with AAV encoding TeNT or presynaptic eGRASP components to (1) silence a subset of CA3 neurons by introducing 0.5 μL of virus directly on CA3 immediately following plating or (2) to abolish GABA release from somatostatin positive interneurons by injecting 1 μL of AAV-Flex-TeNT_{LC} (gift from Hiroki Taniguchi, Max Planck Florida Institute for Neuroscience) into EP7 culture from SST-Cre mice.²⁶ Note that eGRASP_{post} expression is cre-dependent and a plasmid encoding cre recombinase was included in our biolistic transfections.²³ To achieve expression of channelrhodopsin-2, AAV1-EF1-dflox-hChR2(H134R)-mCherry-WPRE-hGH (gift from Karl Deisseroth; Addgene plasmid # 20297) was used. The age of slice culture is reported as equivalent postnatal (EP) day; postnatal day at slice culturing + days *in vitro*.

Adeno-associated virus preparation

Sph-HT-T2A-TeNT, Flex-Sph-HT and eGRASP_{pre}-T2A-TeNT AAV-DJ were generated as previously described.⁴⁸ Briefly, HEK293T cells were co-transfected with the AAV vector along with helper plasmids (pDJ and pHelper) using calcium phosphate transfection. 72 h post-transfection cells were harvested, lysed and purified over an iodixanol gradient column (2 h at 63,500 r.p.m. in a Beckman Type80Ti rotor). Virus was dialyzed to remove excess iodixanol and aliquoted and stored at –80°C until use.

Confocal Ca²⁺ imaging and 1-photon MNI-glutamate uncaging

Live cell imaging of dissociated hippocampal neurons was carried out at 34°C on an Olympus IX71 equipped with a spinning disc scan head (Yokogawa) with a 60x NA1.4 objective. Standard imaging buffer contained (mM) 10 HEPES, 130 NaCl, 5 KCl, 30 days-glucose, 2 CaCl₂ and 1 MgCl₂ supplemented with 1 μM TTX. For uncaging-induced spine growth and Ca²⁺ imaging the same buffer was used, but lacked Mg²⁺ to relieve NMDAR block. Excitation illumination was delivered from an AOTF controlled laser launch (Andor) and images were collected on a 1024x1024 pixel Andor iXon EM-CCD camera. Data acquisition and analysis were performed with Metamorph (Molecular Devices), Andor IQ and ImageJ software. All quantification was performed on raw images, but some images were expanded, using the smooth function in ImageJ for display only. For glutamate uncaging experiments, we included 2 mM MNI-glutamate in the bath solution and focally stimulated the preparation using galvanometric mirrors (FRAPPA, Andor technologies) to steer a diffraction-limited 405 nm spot. An AOTF was used to gate a 500 μs pulse of 405 nm light, with the intensity adjusted to trigger an approximately quantal (10–30 pA) AMPAR current. Intensities ranged from 3 to 4% of total laser power from a 100 mW 405 nm laser that was fiber coupled to an FRAPPA laser scanning unit. NMDAR Ca²⁺ responses were monitored with GCaMP6s (addgene clone #40753). Cells were also transfected with Geph_{FinGR}-mScar and HT-pDisp labeled with JaneliaFluor 646 to identify DiSs. For optical quantal analysis, the frequency and amplitude of spontaneous quantal Ca²⁺ transients were measured at individual DiSs and SiSs as previously described.²⁵ Briefly, neurons were imaged at 5–7 Hz for 2 min before and 5 min following ifenprodil (5 μM , Tocris Bioscience) or at various times (30 s–30 min) following CGP55845 (4 μM , Tocris Bioscience) addition. Quantal events measured at the same spine before and after ifenprodil treatment were averaged (anywhere between 2 and 15 events were averaged, depending on the event frequency at a given spine). For 1-photon (1P) MNI-glutamate induced spine growth, cells expressing mCh along with Geph_{FinGR}-GFP were imaged to identify DiSs and neighboring SiSs. Targeted spines were stimulated with 30 uncaging pulses delivered at 1 Hz (in Mg²⁺-free media). Spine growth was monitored in the GFP channel by imaging z-stacks every 30 s pre- and post-uncaging.

FM dye loading

For FM4-64 experiments, dissociated hippocampal neurons (DIV 17–20) that had been sparsely infected (<50%) with AAV Sph-HT-T2A-TeNT were incubated with 5 μM FM4-64FX (fixable FM dye, Molecular Probes/Thermo) for 1–2 min in normal ACSF containing 10 μM NBQX and 50 μM APV, followed by a 30 s exposure to ACSF containing 50 mM KCl, 5 μM FM4-64FX, 10 μM NBQX and 50 μM APV (NaCl was reduced to 80 mM in this solution to maintain appropriate osmolarity). Cells were returned to normal ACSF

containing 10 μ M NBQX, 5 μ M FM4-64 and 50 μ M APV, incubated for 5 min and then washed with ACSF lacking FM4-64FX but containing 1mM ADVASEP-7 (Sigma). Cells were fixed and processed for VAMP2 staining.

Electrophysiology

Whole-cell recordings (electrode resistance, 5–8 M Ω ; series resistance, 20–40 M Ω) were performed at 30°C on gene-gun-transfected CA1 pyramidal neurons within 40 μ m of the slice surface using a Multi-Clamp 700B amplifier (Molecular Devices). To record uncaging-evoked excitatory postsynaptic currents (uEPSCs), CA1 neurons were patched in voltage-clamp configuration (Vhold of –65 mV and +40 mV for AMPAR-mediated and NMDAR-mediated uEPSCs, respectively) using a cesium-based internal solution (135 mM Cs-methanesulfonate, 10 mM HEPES, 10 mM Na₂ phosphocreatine, 4 mM MgCl₂, 4 mM Na₂-ATP, 0.4 mM Na-GTP, 3 mM Na L-ascorbate, 0.2 mM Alexa Fluor 488, ~300 mOsm, ~pH 7.25) in ACSF containing 2 mM CaCl₂, 1 mM MgCl₂, 0.001 mM TTX, and 2.5 mM MNI-glutamate. uEPSC amplitudes from individual spines were quantified as the average (6–10 test pulses of 1 ms duration at 0.1 Hz) from a 2-ms window centered on the maximum current amplitude after uncaging pulse delivery for AMPA currents and from a 10-ms window between 70 and 80 ms after stimulus for NMDA currents. Laser pulses for uEPSCs were delivered by parking the beam at a point ~0.5 μ m from the center of the spine head (720 nm; 14–15 mW at the sample). Inhibitory postsynaptic currents evoked by two-photon GABA uncaging (uIPSCs) were recorded by patching CA1 pyramidal neurons in the voltage-clamp configuration (Vhold of +10 mV) using a cesium-based internal solution in ACSF containing 2 mM CaCl₂, 1 mM MgCl₂, 0.001 mM TTX, and 0.35 mM RuBi-GABA. Two-photon laser (810 nm) was delivered at a distance of ~0.5 μ m from the center of the spine head at a power of 18–20 mW for a duration of 3 ms with a pulsed Ti:sapphire laser (MaiTai HP, Spectra-Physics). uIPSC amplitudes were quantified as the average (6–10 test pulses at 0.1 Hz) from a 2-ms window centered on the maximum current amplitude within 50 ms after delivery of an uncaging pulse. To assess the role of GABA_BRs in the reduction of NMDAR currents at DiSs, two-color, two-photon uncaging was employed. NMDAR-uEPSCs were acquired in ACSF (2 mM CaCl₂, 1 mM MgCl₂, 0.001 mM TTX, 2.5 mM MNI-glutamate, and 0.35 mM RuBi-GABA; Vhold of +40 mV) from one DiS and one neighboring SiS on the same cell. After a short baseline of NMDAR-uEPSCs, GABA HFU was delivered at the DiS and SiS while the cell was stepped from +40 to –65 mV. Post-GABA HFU NMDAR-uEPSCs were recorded at +40 mV from both DiS and SiS 4–5 min after GABA HFU. GABA high-frequency uncaging (GABA HFU) stimuli consisted of 60 pulses (810 nm; 14–15 mW at the sample) of 2 ms duration delivered at 10 Hz by parking the beam at a point ~0.5 μ m from the center of the spine head. Signals were digitized at 10 kHz and responses were analyzed using Clampfit 10.3 (Molecular Devices) and OriginPro 8.5 software (OriginLab).

Two-photon imaging and high-frequency glutamate uncaging

Imaging was performed at 11–18 days *in vitro* (DIV) on transfected CA1 pyramidal neurons within 40 μ m of the slice surface at 30°C in recirculating artificial CSF (ACSF) (127 mM NaCl, 25 mM NaHCO₃, 1.25 mM NaH₂PO₄, 2.5 mM KCl, 25 mM D-glucose, aerated with 95% O₂/5% CO₂) with 2 mM CaCl₂, 1 mM MgCl₂ and 0.001 mM tetrodotoxin (TTX). For each neuron, image stacks (512 \times 512 pixels; 0.047 μ m/pixel) with 1- μ m z-steps were collected from one segment of secondary or tertiary distal apical dendrites using a two-photon (2P) microscope (Bruker Nano, Inc) with a pulsed Ti:sapphire laser (MaiTai HP; Spectra Physics) tuned to 920 nm (4–5 mW at the sample). For time-lapse imaging, slices were imaged at 2 or 5 min intervals at 30°C in recirculating ACSF. All images shown are maximal projections of three-dimensional image stacks after applying a median filter (2 \times 2) to the raw image data. Two-photon uncaging was achieved as described.²⁶ In brief, LTP-inducing high-frequency 2P glutamate uncaging stimulus (Glu HFU) consisted of 30 pulses (720 nm; 15–18 mW at the sample) of 5 ms duration delivered at 1 Hz by parking the beam at a point ~0.5 μ m from the center of the spine head with a pulsed Ti:sapphire laser (MaiTai HP, Spectra-Physics) in at 30°C in ACSF containing (in mM): 3 Ca²⁺, 0 Mg²⁺, 0.001 TTX, and 2.5 mM MNI-glutamate.⁴⁹ No more than two Glu HFU trials were performed from the same neuron.

Optogenetic IPSCs

Optically evoked IPSCs (oIPSCs) were recorded by patching CA1 pyramidal neurons in SST-Cre hippocampal slices infected with AAV1-EF1-dflox-hChR2(H134R)-mCherry-WPRE-hGH or co-infected with AAV1-EF1-dflox-hChR2(H134R)-mCherry-WPRE-hGH and AAV-Flex-TeNT_{LC}. Voltage-clamp configuration (Vhold of +10 mV) was achieved using a cesium-based internal solution in ACSF containing 2 mM CaCl₂, 1 mM MgCl₂. oIPSCs were evoked by full-field illumination (100ms, 470nm, 7–8mW, Thorlabs) and quantified as the average (10 pulses at 0.2 Hz) of maximum current amplitude within 50ms after delivery of a blue light pulse.

Pharmacology

Stocks were prepared at 1,000 \times (or greater) by dissolving Tetrodotoxin citrate, (R)-CPP, and Bicuculline methochloride in water; CGP55845 in DMSO. All drugs were from Tocris unless otherwise noted.

QUANTIFICATION AND STATISTICAL ANALYSES

Image analysis and quantification

Estimated spine volume and gephyrin enrichment on dendritic spines were measured in fluorescence images from red (tdTomato) and green (GFP) channels using ImageJ (NIH). Integrated fluorescence intensities were calculated from background-subtracted and bleed-through-corrected red and green fluorescence using the integrated pixel intensity of a boxed region (ROI) surrounding

the spine head, as described previously.^{8,26} Gephyrin enrichment in DiS was calculated by normalizing GFP-gephyrin fluorescence intensities (as described above) for each punctum to the mean GFP fluorescence intensity determined from four background ROIs on the same dendritic shaft. GFP-gephyrin enrichment was considered to be a gephyrin punctum when the ratio of green from a punctum of DiS to green from dendritic background (Gs/Gd) was >1. “DiS” (expression level >mean; Gs/Gd > 1) versus “SiS” (expression level <mean; Gs/Gd < 1). <https://github.com/mjkennedylab/DualSynapse>.

Uncaging evoked IPSCs and EPSCs

uEPSC amplitudes from individual spines were quantified as the average (6–10 test pulses of 1 ms duration at 0.1 Hz) from a 2-ms window centered on the maximum current amplitude after uncaging pulse delivery for AMPA currents and from a 10-ms window between 70 and 80 ms after stimulus for NMDA currents. uIPSC amplitudes were quantified as the average (6–10 test pulses at 0.1 Hz) from a 2-ms window centered on the maximum current amplitude within 50 ms after delivery of an uncaging pulse.

Optogenetically evoked IPSCs

oIPSCs were evoked by full-field illumination (100ms, 470nm, 7–8mW, Thorlabs) and quantified as the average (10 pulses at 0.2 Hz) of maximum current amplitude within 50ms after delivery of a blue light pulse. Data from at least three independent slice culture preparations were used for two-photon imaging experiments.

Statistical analyses

All electrophysiology, staining and calcium imaging data were analyzed in Graphpad Prism. Generally, we used Student's t test for comparisons between groups unless otherwise noted in figure legends with statistical significance set at $p < 0.05$. In cases where data were compared from the same cell/synapse pre/post treatment, we used paired Student's t test, as noted in the figure legends. Values for technical and experimental replicates are listed in the figure legends. For serial reconstruction EM data, we checked data for normality with Kolomogorov-Smirnov test and found only the size of symmetric synapses in SLM to be consistent with normal distribution. Thus, we used unpaired two-tailed t test to compare DiS and shaft in this layer (Figure S1B, SLM - symmetric). Synapse sizes in other categories were not distributed normally, so we used Kruskal-Wallis test for asymmetric synapses in SR and SLM, and Mann-Whitney test for symmetric synapses in SR (Figures S1A and S1B). We pooled together the dendrite and synapse size data from all conditions in SR (i.e., control, LTP, and perfusion-fixed) since DiSs were rare in this layer in adult rat CA1.